

A HYPERSPECTRAL VIEW OF THE CRAB NEBULA

M. CHARLEBOIS^{1,2}, L. DRISSSEN^{1,2}, A.-P. BERNIER^{1,2}, F. GRANDMONT³, AND L. BINETTE⁴

¹ Département de Physique, de Génie Physique et d'Optique, Université Laval, Québec, Québec G1V 0A6, Canada; maxime.charlebois.1@ulaval.ca, ldrissen@phy.ulaval.ca, anne-pier.bernier.1@ulaval.ca

² Centre de Recherche en Astrophysique du Québec, Canada

³ ABB Bomem Inc., 585 boulevard Charest est, Suite 300, Québec, Québec G1K 9H4, Canada

⁴ Instituto de Astronomía, UNAM, Ap.70-264, 04510 México, DF, Mexico

Received 2009 July 29; accepted 2010 March 11; published 2010 April 9

ABSTRACT

We have obtained spatially resolved spectra of the Crab nebula in the spectral ranges 450–520 nm and 650–680 nm, encompassing the H β , [O III] λ 4959, λ 5007, H α , [N II] λ 6548, λ 6584, and [S II] λ 6717, λ 6731 emission lines, with the imaging Fourier transform spectrometer SpIOMM at the Observatoire du Mont-Mégantic's 1.6 m telescope. We first compare our data with published observations obtained either from a Fabry–Perot interferometer or from a long-slit spectrograph. Using a spectral deconvolution technique similar to the one developed by Čadež et al., we identify and resolve multiple emission lines separated by large Doppler shifts and contained within the rapidly expanding filamentary structure of the Crab. This allows us to measure important line ratios, such as [N II]/H α , [S II]/H α , and [S II] λ 6717 / [S II] λ 6731 of individual filaments, providing a new insight on the SE–NW asymmetry in the Crab. From our analysis of the spatial distribution of the electronic density and of the respective shocked versus photoionized gas components, we deduce that the skin-less NW region must have evolved faster than the rest of the nebula. Assuming a very simple expansion model for the ejecta material, our data provide us with a complete tridimensional view of the Crab.

Key words: instrumentation: spectrographs – ISM: supernova remnants – radiation mechanisms: general – supernovae: individual (SN 1054) – techniques: radial velocities

Online-only material: animation, supplementary data

1. INTRODUCTION

As one of the youngest and nearest Galactic supernova remnants, the Crab Nebula (M1) is a key object for studying the complex physics involved in the first centuries following a supernova explosion. Observations of the Crab are therefore numerous and today cover all wavelengths. Through the use of space telescopes, new data have been gathered during the last decade, with the aim of studying the details of its filamentary structure at high spatial resolution (*Hubble Space Telescope* (*HST*): Sankrit et al. 1998; Loll et al. 2007), its dust content and the morphology of the synchrotron infrared emission (*Spitzer*: Temim et al. 2006), or its X-ray spectrum (*XMM-Newton*: Kaastra et al. 2009).

Visible-band spectroscopy of individual filaments, as well as long-slit coverage of a significant fraction of the entire nebula (see, for instance, Davidson & Fesen 1985; MacAlpine et al. 1996, or Čadež et al. 2004) have revealed a highly diversified filamentary structure in terms of line ratios and velocity field. Because the ejected material is still expanding at large velocities ($\sim 1500 \text{ km s}^{-1}$) and because of the numerous overlapping filamentary structures, a complete mapping of individual emission lines in the nebula is nevertheless difficult and significantly complexifies the analysis. MacAlpine et al. (1996) have identified a general NW–SE asymmetry in the distribution of nitrogen-rich and sulfur-rich filaments using a series of long slit spectra. Recently, Čadež et al. (2004) obtained high-resolution long-slit spectra of the Crab along ten different orientations across the nebula, revealing its tridimensional structure.

The detailed review of the Crab Nebula by Hester (2008) is a clear and vibrant testimony to the complex interaction between the pulsar, the synchrotron emission, and the rapidly expanding

ejecta; we refer the reader to this paper for a thorough overview of this fascinating object.

Because of its complicated three-dimensional filamentary structure shaped by the rapid expansion of the nebula, the Crab was seen as a target of choice to demonstrate the capabilities of our new integral field spectrometer Spectromètre Imageur de l'Observatoire du Mont-Mégantic (SpIOMM). SpIOMM's large field of view, which encompasses the entire Crab, provides the first truly integral field spectroscopic observations of this object in eight emission lines. After a short description of the instrument and the observations (Section 2), we compare some of our results with those obtained with more conventional instruments with the aim of establishing the validity of our techniques and results (Section 3.1), we then present the spectral deconvolution technique applied to the data cube (Section 3.2) that made possible a three-dimensional mapping of the individual emission lines (Section 3.3). In Section 4, we present an interpretation of our results. Finally, we present (Section 5) a three-dimensional model of the Crab nebula based on our data and assuming a simple expansion law.

2. OBSERVATIONS

The data presented in this paper were obtained in 2007 November with the imaging Fourier transform spectrometer SpIOMM (Grandmont et al. 2003; Drissen et al. 2008; Bernier et al. 2008; F. Grandmont et al. 2010, in preparation) attached to the 1.6 m telescope of the Observatoire du Mont-Mégantic. This instrument acquires the spectrum, in the visible range (350–900 nm), of every source of light in a 12' circular field of view, with a spatial resolution limited by the seeing, typically 1''.5, and a spectral resolution ranging from $R = 1$ (deep panchromatic image) to $R = 25,000$.

Table 1
Characteristics of the Red and Blue Data Cubes

Characteristic	Blue	Red
Spectral range	450–520 nm	650–680 nm
Alias order	6	16
OPD sampling distance	1582 nm	5542 nm
Exposure time per image	35 s	30 s
Number of images	118	413
Resulting resolution	68.0 cm ⁻¹	7.92 cm ⁻¹
Total observation time	85 minutes	261 minutes

Spectral information is obtained by acquiring multiple panchromatic images of the selected scene that are modulated in intensity in a precisely controlled fashion. The core of the instrument is a Michelson interferometer inserted in series within the camera optical design, which modulates the image intensity from total dark to total brightness depending on the optical path difference (OPD) between the two interferometer arms. A recording of these panchromatic images generated at equally spaced OPD positions creates the raw data cube, thus producing a discrete interferogram for each pixel of the image from which spectral information can then be extracted. The detector is a Princeton Instrument EEV CCD camera with 1340×1300 pixels (0.55 each); the data, however, are binned 2×2 during readout in order to reduce the readout time to less than 4 s.

The spectrum of the source, at each pixel, is obtained from the Fourier transform of these individual interferograms. Before transforming the interferograms, classical data reduction (bias subtraction and flatfield correction) was performed on every image. Also, because of imperfect guiding during the collection of the data cube, all images were then aligned with each other by measuring the centroid of a dozen stars in the field. The maximum displacement between the first and the last images was found to be less than 2 pixels. We also corrected the interferogram for the slightly varying sky transparency (a few percent) using photometry of stars outside the nebula. These reduced interferograms are then ready for Fourier transformation. In order to minimize spectral line blending confusion, a Gaussian apodization is applied to the interferogram, which is subsequently Fourier transformed. The result is then spectrally calibrated (using a high-resolution data cube of a reference He–Ne laser at 6328 Å) and interpolated in order to fit the same spectral grid for every pixel. Thus, every pixel of the image contains a spectrum and all the spectra share the same spectral grid. There is no need to calibrate these spectra using the spectral sensitivity curve of the detector since its variation has been measured to be negligible over the spectral intervals used here. All these reductions were performed with IDL, although similar tasks are also available in IRAF.

SpIOMM is based on the same principle as BEAR, the Canada–France–Hawaii’s imaging Fourier transform spectrometer, although with a different field of view and wavelength range (see Noel et al. 2005, or Paumard et al. 2004 for a description of data obtained with BEAR). Because SpIOMM and BEAR data essentially consist of images, there is no need for complex image reconstruction techniques as in the case of integral field units, image slicers, or a series of long slits.

In order to reduce the total number of steps and the background noise while keeping a moderate spectral resolution, we have used a standard spectral folding technique combined with two interference filters isolating the most prominent emission

lines. Two data cubes were thus obtained: H β and [O III] λ 4959, λ 5007 which were observed with a blue filter (spectral coverage 450–520 nm; $R = 300$), while H α , [N II] λ 6548, λ 6584 and [S II] λ 6717, 6731 were observed with a red filter (covering the 650–680 nm range; $R = 1800$). The average seeing during the observations was 2". Table 1 summarizes the observing parameters of those two data cubes.

The final data cubes (R.A., decl., λ) consist of 435,500 spectra with 118 and 413 spectral resolution elements for the blue and red cubes, respectively; since the nebula spans about 5' on a side, only about 100,000 spectra contain meaningful information.

3. RESULTS

3.1. Comparison with Previous Work

Because this is the first SpIOMM data set published, we first compare our results with previously published data on the Crab nebula in order to establish the validity of our techniques and results before proceeding with the analysis.

First, monochromatic images (defined by the selected spectral resolution), or groups of images summed over any desired wavelength intervals, can be extracted from the reduced SpIOMM’s data cubes. In the case of the Crab, however, because of the large Doppler shifts introduced by the expansion of the nebula, images of individual emission lines are not really monochromatic but rather span the entire wavelength range dictated by the Doppler shift, unavoidably mixing adjacent lines. This Doppler mixing will be deconvolved later in this paper. We therefore show in Figure 1 various images centered on the most prominent emission lines, as well as of the adjacent continua. In these images, the two strong lines of [O III], the H α , and the two [N II] lines, as well as the two lines from the [S II] doublet are grouped together. We note an excellent agreement with images obtained with WFPC2, in particular in the light of the [S II] λ 6717, 31 and [O III] λ 4959, λ 5007 lines (see Sankrit et al. 1998; their Figures 2 and 3, respectively). Subsequently, SpIOMM can also be used in a mode similar to that of a low-resolution, broadband Fabry–Perot. The best available comparison with our data is provided by Lawrence et al. (1995), who have obtained a F–P cube of the Crab of the [O III] 5007 line with a resolution of $R = 945$. The spectral resolution of our blue cube ($R = 300$, or 17 Å) is much lower than that of Lawrence et al., but is sufficient to resolve the two strong lines from [O III]. Moreover, the expansion velocity of the nebula being ~ 1500 km s⁻¹, there is very little overlap between the redshifted 4959 Å component and the blueshifted 5007 Å one. Since there is practically no spectral blending, contrary to the red cube, we can present the data without further processing. Figure 2 shows the [O III] λ 5007 line as seen through nine velocity channels of the cube, while Figure 3 illustrates the expansion of the nebula through a color-coded map obtained by assigning the *B*, *V*, and *R* colors to the sum of images from the blueshifted, central, and redshifted channels of this line, respectively. Although the spectral resolution of our blue cube is much lower than that available with Fabry–Perot interferometers, the mosaic in Figure 2 shows remarkable similarities with the data presented by Lawrence et al. (1995; their Figure 2).

Alternatively, spectra integrated over specific regions of interest can also be extracted from the cube. The spectral resolution of the red cube, with a typical FWHM ~ 3.8 Å ($R = 1800$), is about 1.6 times better than that of the “low resolution” spectra presented by Čadež et al. (2004). Within the range covered by the red filter, five lines are clearly detected:

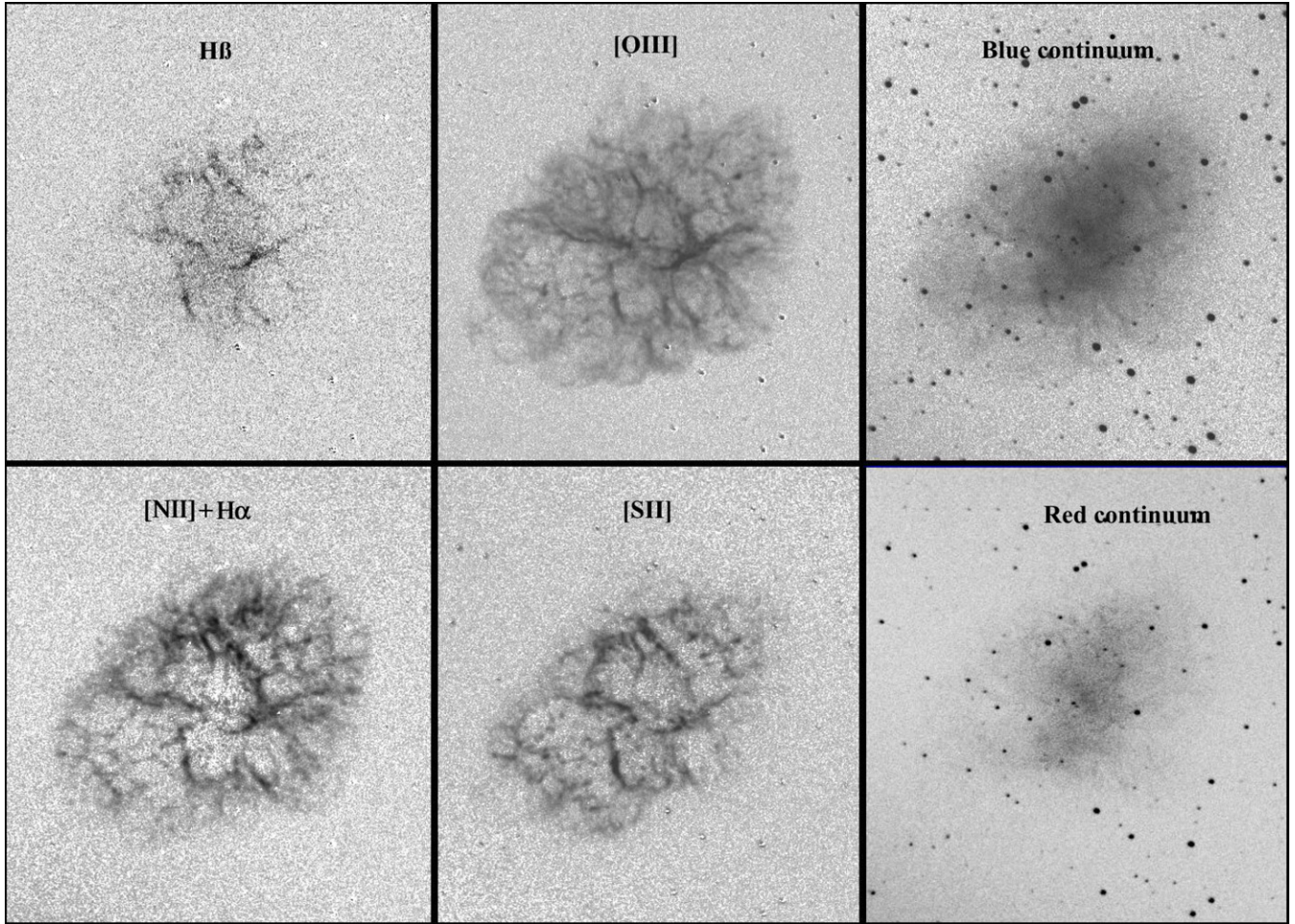


Figure 1. Images of the most prominent emission lines and of the related continuum from the blue (upper panels) and red cubes (lower panels) of the Crab nebula. Images spanning the entire velocity range were averaged for each line, and the continuum was subtracted from the emission line images. Because of line overlapping and Doppler crossing, images of the [N II] $\lambda 6548$, H α , and [N II] $\lambda 6584$ were combined, as well as the two components of the [S II] $\lambda\lambda 6717, 31$ line pair. Images are $6'.5 \times 6'.9$, with north at the top and east to the left.

[N II] $\lambda 6548$, H α , [N II] $\lambda 6584$, [S II] $\lambda 6717$, and [S II] $\lambda 6731$. We see no evidence for the He I $\lambda 6678$ line above the noise level. Contrary to the lines within the blue range, these spectral lines are all subject to strong blending as a result of the Doppler shift caused by the rapid expansion. The spectrogram displayed in Figure 4, extracted from a region where two filaments are expanding in opposite directions, overlap, which illustrates the complexity of the kinematical features seen in M1. In this case, all the lines are clearly separated, with the notable exception of the overlapping blueshifted [N II] $\lambda 6584$ and redshifted [N II] $\lambda 6548$, which cannot be separately resolved.

As a last comparison, we note that one can mimic the use of a long slit by cutting a slice through the SpIOMM data cube. This is illustrated in Figure 5, where we show the spectrum of the Crab as seen through a 1 pixel wide ($1''.1$) N–S “slit” centered on the pulsar. This corresponds to the $\psi = 90^\circ$ slit in Čadež et al. (2004), whose spectrum appears in their Figure 7. Again, we note an excellent agreement between the SpIOMM data and the traditional long-slit spectrogram.

3.2. Spectral Deconvolution

Our main purpose with these data is the measurement of line ratios from individual filaments, in order to determine their abundances and the electron density. In order to do so,

it is essential to clearly identify these individual filaments in spatial as well as in velocity space, a task made possible by the Doppler shift caused by the expansion of the material. However, this requires a spectral deconvolution technique that we now describe in details; note that we have only processed the red cube with this technique, as it is applied to every single spectrum in the cube.

The spectrum shown in Figure 4 is relatively simple in the sense that the lines emitted by the two filaments can easily be identified. This is not always the case however, because in occasion more than two filaments overlap on a given pixel/spectrum or because the Doppler shifts make line identifications ambiguous, or a combination of both effects. Examples of these spectra are shown in the upper panel of Figure 6, with the spectrum on the left being very similar to the one shown in Figure 4 and the other one being more difficult to interpret. From these spectra, we can see that the five lines are duplicated due to the presence of two filaments expanding at different velocities along the line of sight, thus producing a total of ten overlapping spectral lines.

Due to the large number of spectra (about 100,000 covering the whole nebula) and the ambiguity of line identification, we needed to build an algorithm that could correctly identify these spectral lines, measure their intensity, and their spectral shift. Our algorithm is based on a technique similar to the one

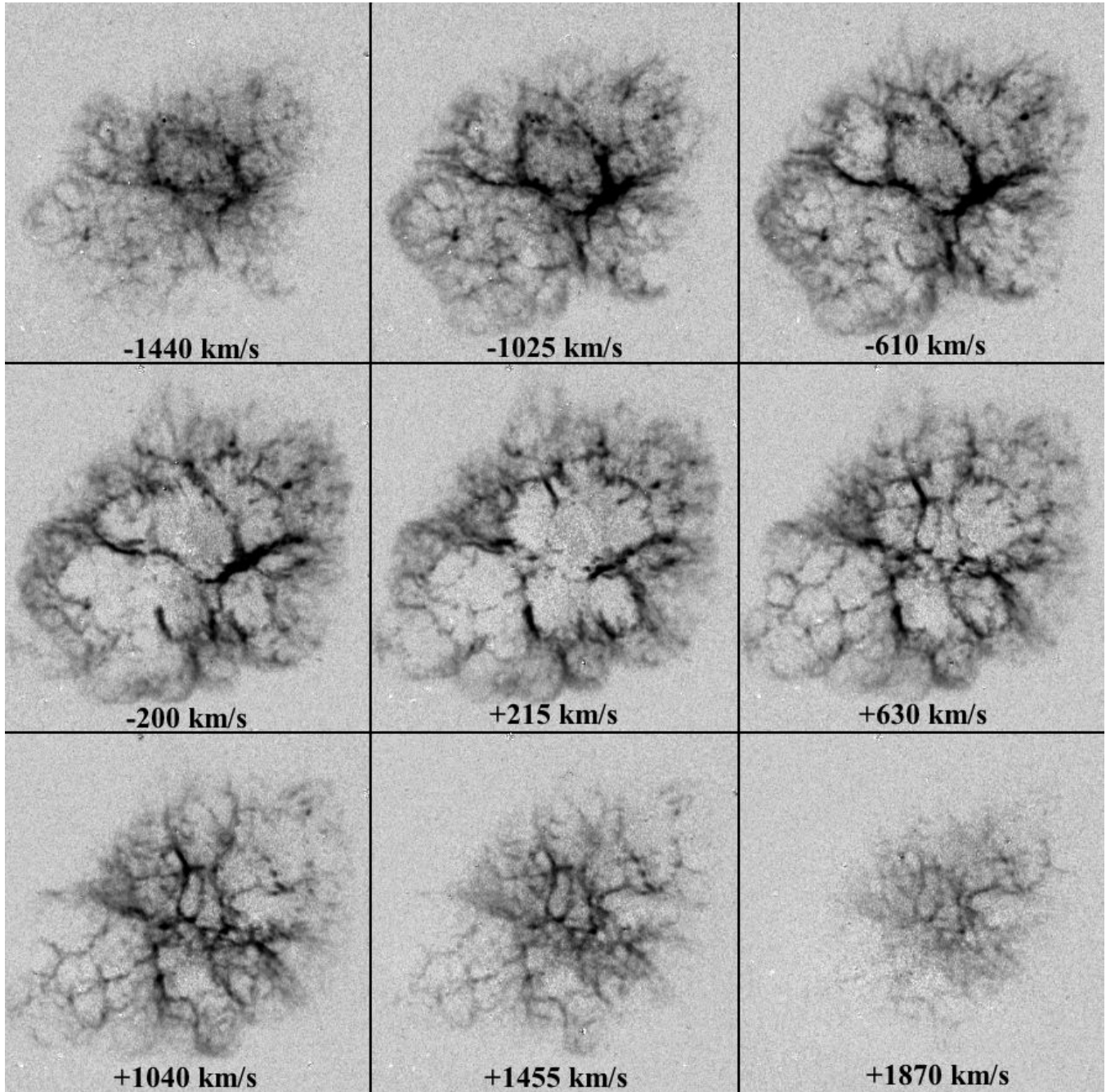


Figure 2. Mosaic of the section of the blue data cube covering the [O III] $\lambda 5007$ line. The underlying continuum was subtracted. Note the classical “cage-like” structure surrounding the synchrotron emission which can be seen in the right-hand panels of Figure 1. Each panel is 5'5 on a side, with north at the top and east to the left.

developed by Čadež et al. (2004). Indeed, for each of the five lines identified above (Table 2), using the associated laboratory wavelength λ_i , we define a probability w_i of finding emitting matter at a radial velocity v along the line of sight of the concerned spectrum. Considering the information that we can retrieve from individual lines separately, this probability is equal to the amplitude of the spectrum expressed in velocity scale. This is equivalent to performing the integral transform of the spectral distribution $S(\lambda)$ with a Gaussian kernel Doppler-shifted to a particular velocity v :

$$w_i(v) = \int_{-\infty}^{\infty} S(\lambda) \exp\left(-\frac{(\lambda - \lambda_i(1 + v/c))^2}{2\sigma^2}\right) d\lambda,$$

where 2.355σ is taken to be representative of the mean spectral line FWHM. Thus, for each line i , we obtain a different probability $w_i(v)$ of finding an emitting filament at the radial velocity v . We then take advantage of the fact that the combined probability of finding two lines of the same species is much more reliable. Indeed, since [N II] $\lambda 6548$ is always accompanied by [N II] $\lambda 6584$ and [S II] $\lambda 6717$ by [S II] $\lambda 6731$, the multiplication of their individual probabilities $w_i(v)$ is a very good indicator of the presence of emitting matter at velocity v . Then, like Čadež et al. (2004), we define a global probability $\Omega(v)$ of finding an emitting filament at velocity v as follows:

$$\Omega(v) = w_1(v)w_2(v) + w_c(v)w_3(v) + w_4(v)w_5(v).$$

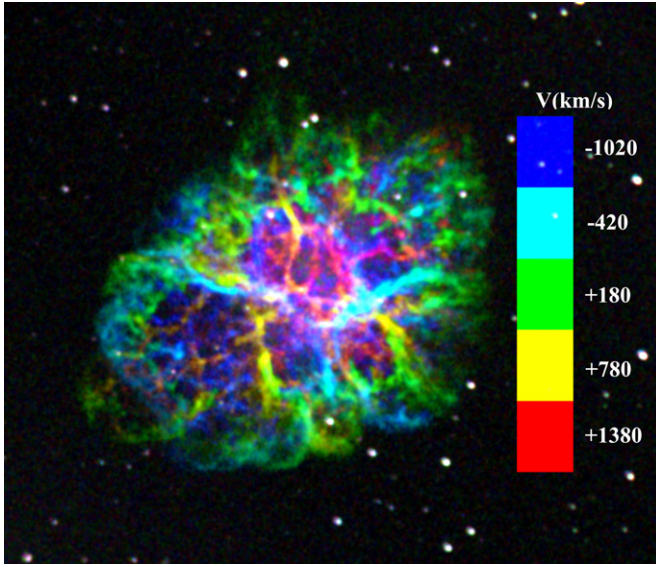


Figure 3. Color-coded velocity map of the [O III] $\lambda 5007$ line.

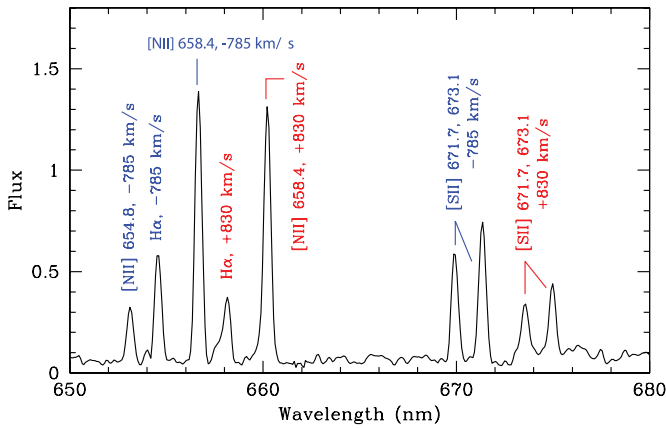


Figure 4. Representative spectrogram (average of 10 pixels) extracted from the red cube. Two groups of lines are clearly seen, a typical signature of two overlapping filaments on the line of sight. Note that the redshifted [N II] $\lambda 6548$ line, not indicated on the graph, is superimposed on the blueshifted [N II] $\lambda 6584$ component.

Since $H\alpha$ is not part of a line pair, we set $w_c = 0.5(w_2 + w_5)$. The $\Omega(v)$ found for the two spectra of the upper panel of Figure 6 is shown in the middle panel of the same figure. We have to keep in mind that $\Omega(v)$ is foremost a tool to find the true Doppler shift and that it can sometimes create artificial maxima, like the one at 0 km s^{-1} in Figure 6 (left part of mid panel) and the other at 750 km s^{-1} in the right panel. These artificial structures arise when two filaments overlap in the same line of sight and coincidentally have a Doppler velocity separation corresponding to the wavelength separation of the [N II] or [S II] line pairs.

Using these $\Omega(v)$ profiles (for each pixel), we proceed to identify three maxima that can then be tested to fit theoretical spectra. To each $\Omega(v)$ maximum corresponds a set of five theoretical lines (see Table 2), which are simultaneously fitted applying the same Doppler shift as the corresponding $\Omega(v)$ maximum. Unlike Čadež et al. (2004), we simultaneously fit all the potential lines instead of doing it sequentially. The relative heights of these maxima are then used as an initial guess for the line amplitudes. An iterative procedure is then applied, which converges to an improved fit of the three five lines systems. We have limited our search technique to three overlapping filaments only due to the limitations imposed by the signal-to-noise ratio

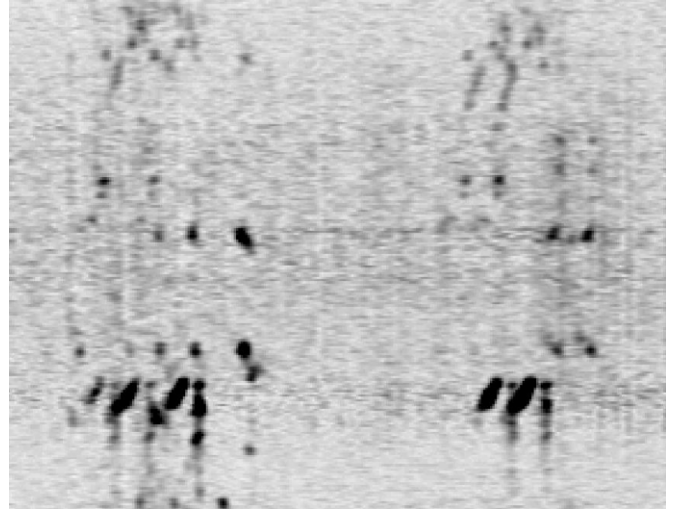


Figure 5. Two-dimensional cut through the nebula extracted from the red data cube, mimicking a long-slit ($4'5$ long) spectrogram (from 6500 \AA on the left to 6800 \AA on the right), in the N–S direction and centered on the pulsar. North is at the top, south at the bottom. To be compared with Figure 7 from Čadež et al. (2004), showing the spectrum obtained with a classical dispersive spectrograph through a real long-slit having the same length and orientation.

Table 2
Line Identification Used in the Deconvolution

i	Line	λ_i (nm)
1	[N II]	654.8
2	[N II]	658.4
3	$H\alpha$	656.3
4	[S II]	671.7
5	[S II]	673.1

(S/N) and by the finite spectral and spatial resolution of our data.

To minimize the fitting parameters of the algorithm, we do not leave the spectral width free to vary, since it is rather constant (3.8 \AA) over all the spectra. We also take advantage of the fact that the ratio between [N II] $\lambda 6548$ and [N II] $\lambda 6584$ must be constant (and equal to 3; Storey & Zeippen 2000). Then, there are only 3 times four amplitudes to fit, giving us a total of 12 free parameters. Minimizing the number of fitting parameters makes it more likely to find a unique and reliable solution to a least square fitting algorithm. This way, the IDL's algorithm CURVEFIT is able to extract the spectral parameters that yield the absolute minimum in χ^2 -space. The solutions obtained for the spectra displayed in the upper panels of Figure 6 are shown in the lower panels of the same figure.

This procedure is then applied to the spectrum of each and every pixel of the red data cube in order to obtain a deconvolved integral spectrum of the entire nebula that will lead us to produce the results presented in the next section. An example of the deconvolution process on a series of ~ 160 spectra corresponding to a $3'$ long slit is shown in Figure 7 (left panel). The filamentary structure, curved and elongated in velocity space, is successfully recovered after deconvolution, as seen in the right panel.

3.3. Maps of Line Intensities and Line Ratios

Once the spectra have been deconvolved, a cube of the intensity maps at different velocities can be produced for the $H\alpha$, [N II] $\lambda 6584$, and [S II] $\lambda \lambda 6717, 31$ lines. For each

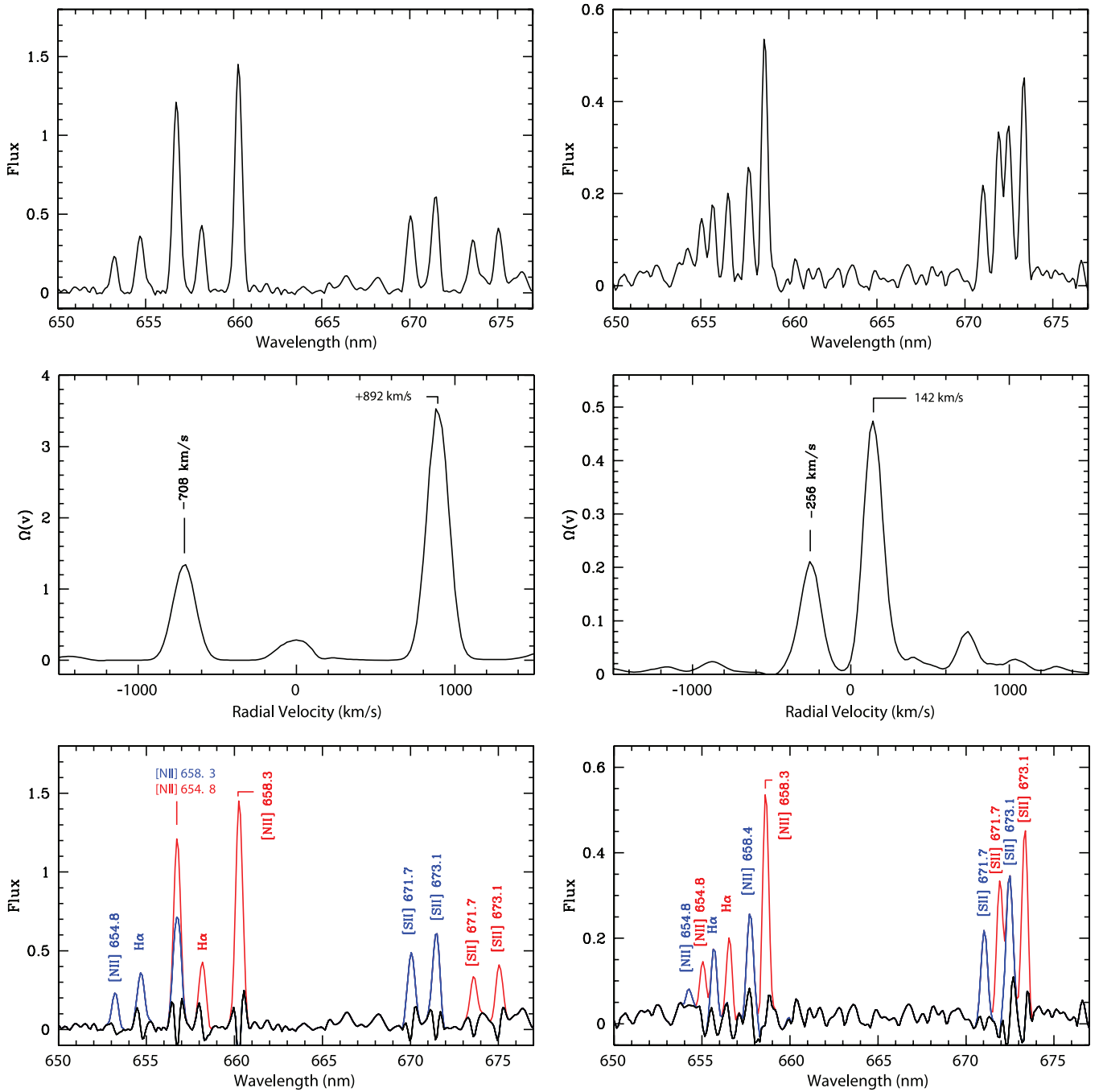


Figure 6. Upper panels: examples of spectrum extracted from 1 pixel of the red data cube of M1. Middle panels: $Q(v)$ obtained for the spectra from the upper panels. Lower panels: deconvolved spectra. The red spectrum is the original one. The blue spectrum is obtained after subtraction of the brightest filament's fitted emission. The black spectrum is the residual of the fit.

line, we initially oversampled in velocity space the reconstructed spectra by choosing channels that are separated by only 20 km s^{-1} . We keep only channels between $\pm 1600 \text{ km s}^{-1}$ since only these contain relevant information. This velocity interval also corresponds to the maximum ejection velocity measured along our line of sight.

A mosaic of the $[\text{N II}] \lambda 6584$ data cube thus obtained is shown in Figure 8. Each image of the mosaic is the average of ten spectral elements of the reconstructed data cube, ranging from -1500 km s^{-1} on the top left corner to $+1500 \text{ km s}^{-1}$ at the bottom-right corner. It is apparent from this figure (see first

three, and last three channels), as noted by Lawrence et al. (1995) and also from Figure 2 (which shows the expansion velocity of the nebula in the $[\text{O III}]$ line), that the most extreme velocities are found in the NW section of the nebula. This is quantified in Figure 9, where we show the radial velocity defined by the $[\text{N II}] \lambda 6584$ line, as a function of the distance from the pulsar, along an axis perpendicular to the Crab pulsar wind torus (P.A. = 126° as found by Ng & Romani 2004).

The spatial distribution of $\text{H}\alpha$ and $[\text{S II}]$ emission is globally similar to that of $[\text{N II}]$ but the line ratios present some interesting variations. To illustrate this, we present, in Figures 10–12, three

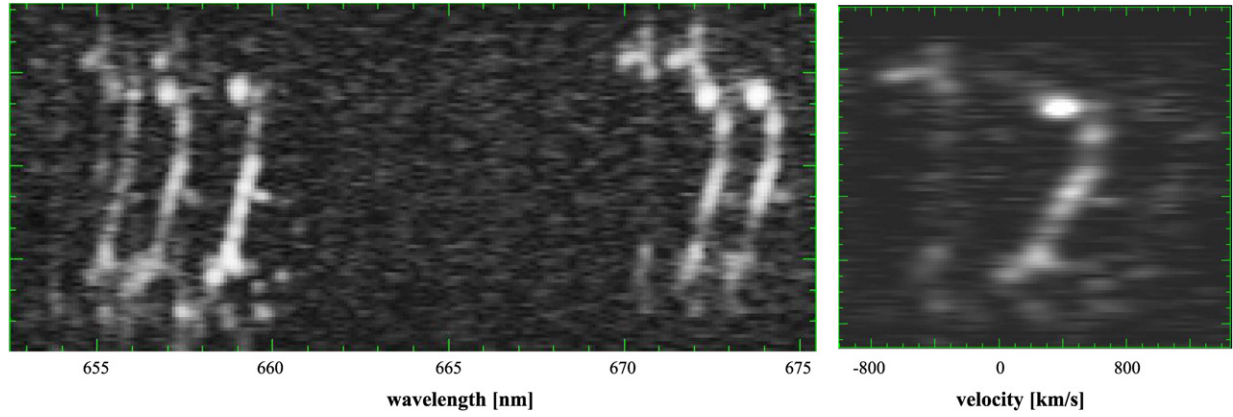


Figure 7. Spectrum obtained through an artificial long-slit extracted from the red data cube (left) and the resulting $\Omega(v)$ (right) calculated from the line system inferred from the long-slit spectrum on the left. Each of the five spectral line structures that can be observed on the left-hand spectrum appears clearly as one bright filamentary structure on the right-hand panel.

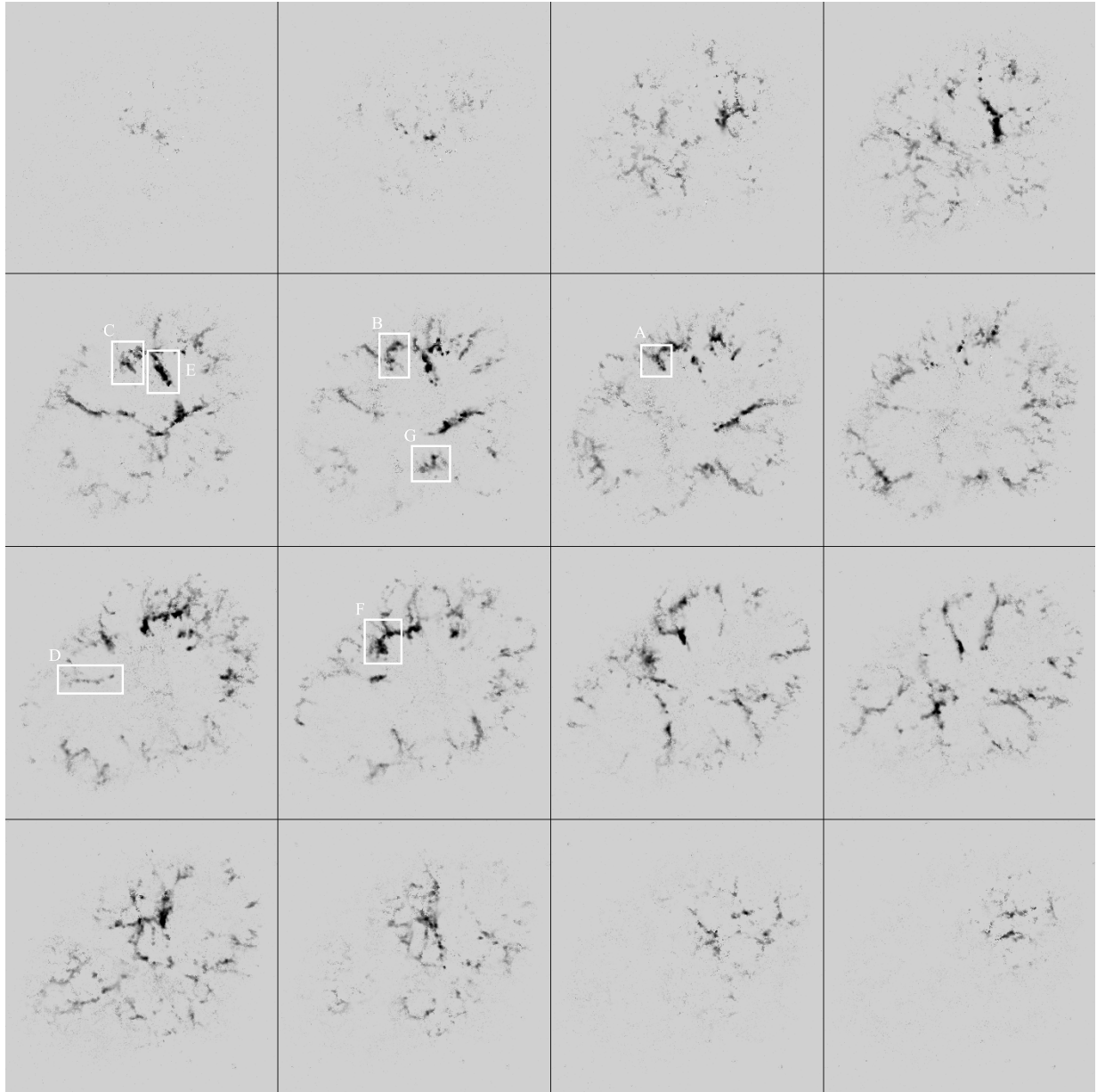


Figure 8. Mosaic of the $[\text{N II}] \lambda 6584$ emission line. It presents the ten frames average of the $[\text{N II}] \lambda 6584$ cube resulting from the algorithmic processing described in the text. Top left is the first averaged frame at a mean velocity of -1500 km s^{-1} . From left to right, there is a 200 km s^{-1} increase for each frame, up to the last frame (bottom right), which has a mean velocity of $+1500 \text{ km s}^{-1}$.

(A full resolution version of this figure is available in the online journal.)

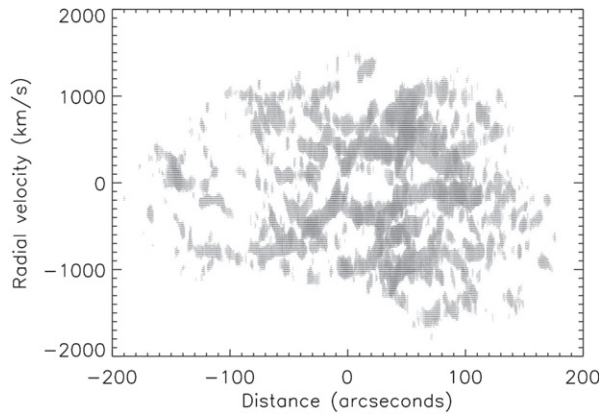


Figure 9. Radial velocity of the gas as a function of the distance from the pulsar. This plot has been constructed by calculating the projection of every voxel that contains a S/N above 7 in the [N II] cube on the plane coplanar with the line of sight (velocity axis) and the pulsar axis (P.A. = 126°31', see Ng & Romani 2004). Negative distances thus refer to pixels located in the SE portion of the nebula, while positive distances are in the NW part.

mosaics showing the velocity-resolved line ratios [N II]/H α , [S II]/H α , and [S II] λ 6717/[S II] λ 6731.

These ratio maps were calculated from the individual line intensity cube discussed above. Rola & Pelat (1994) argued that the minimum S/N required for each line to yield a significant line ratio is 6. In our case, since the cube contains a lot of information in the spatial domain as well, we consider that a sufficient criterion to calculate a line ratio is that at least one of the two spectral lines used in the ratio must have a minimum S/N of 7. Once such cube is obtained, we can average it 10 frames by 10 frames (by considering only the voxels that respect the S/N criterion established above) and subsequently produce a map of the cube for different velocity channels. For all our maps, we selected a color contrast which optimizes the information presented. The range chosen is bounded by threshold values over which the ratio is still relevant but with too large uncertainties due to the specific choice of S/N criterion. For example, a ratio of 4.0 in Figure 11 can be perceived as a ratio that is at least 4.0, but was measured to be higher (up to almost 10.0).

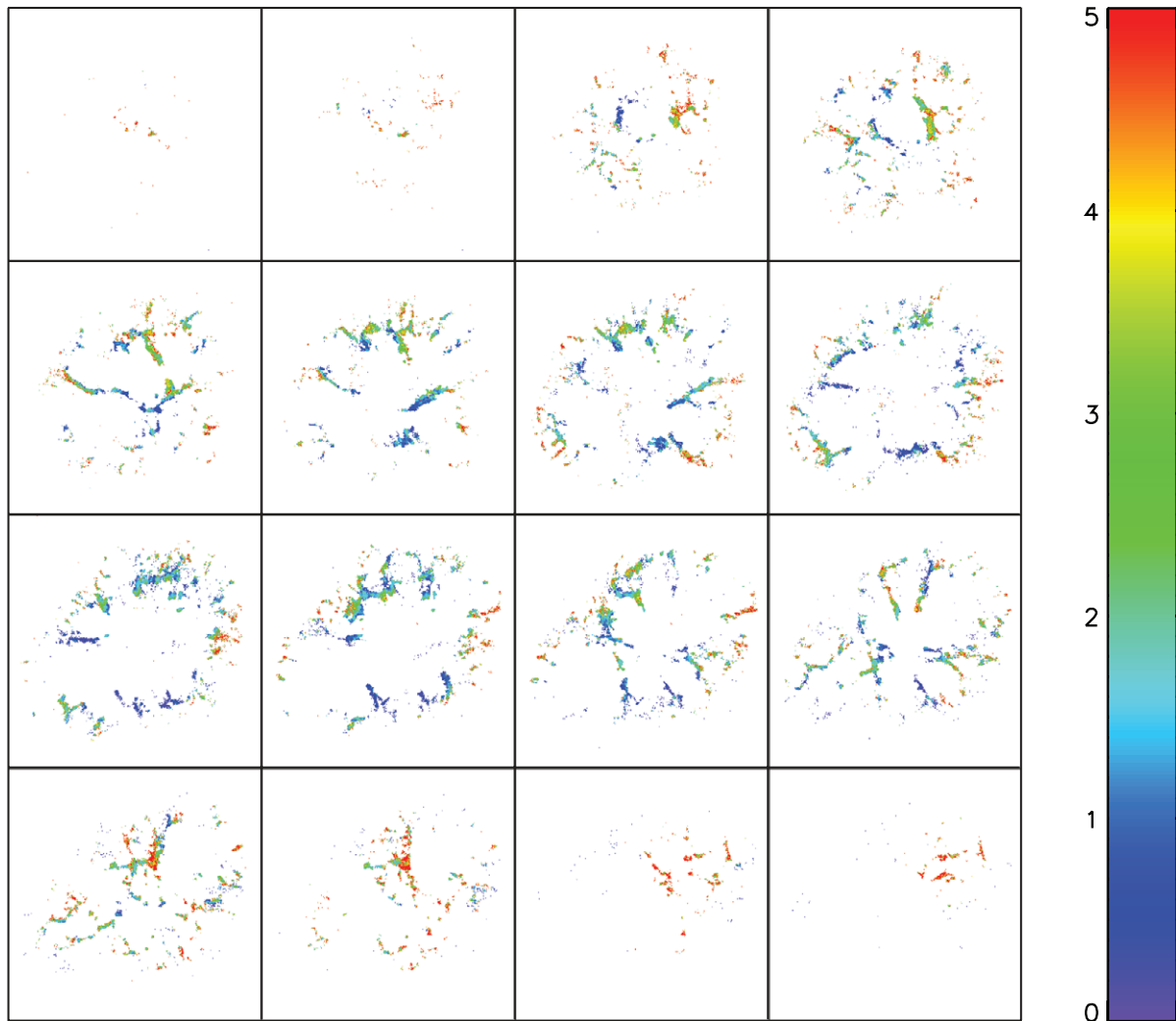


Figure 10. [N II]/H α line ratio calculated from the ratio of every voxel containing a S/N ≥ 7 in either of the spectral lines. The mean velocity for each map of the mosaic is the same as in Figure 8.

(A full resolution version of this figure is available in the online journal.)

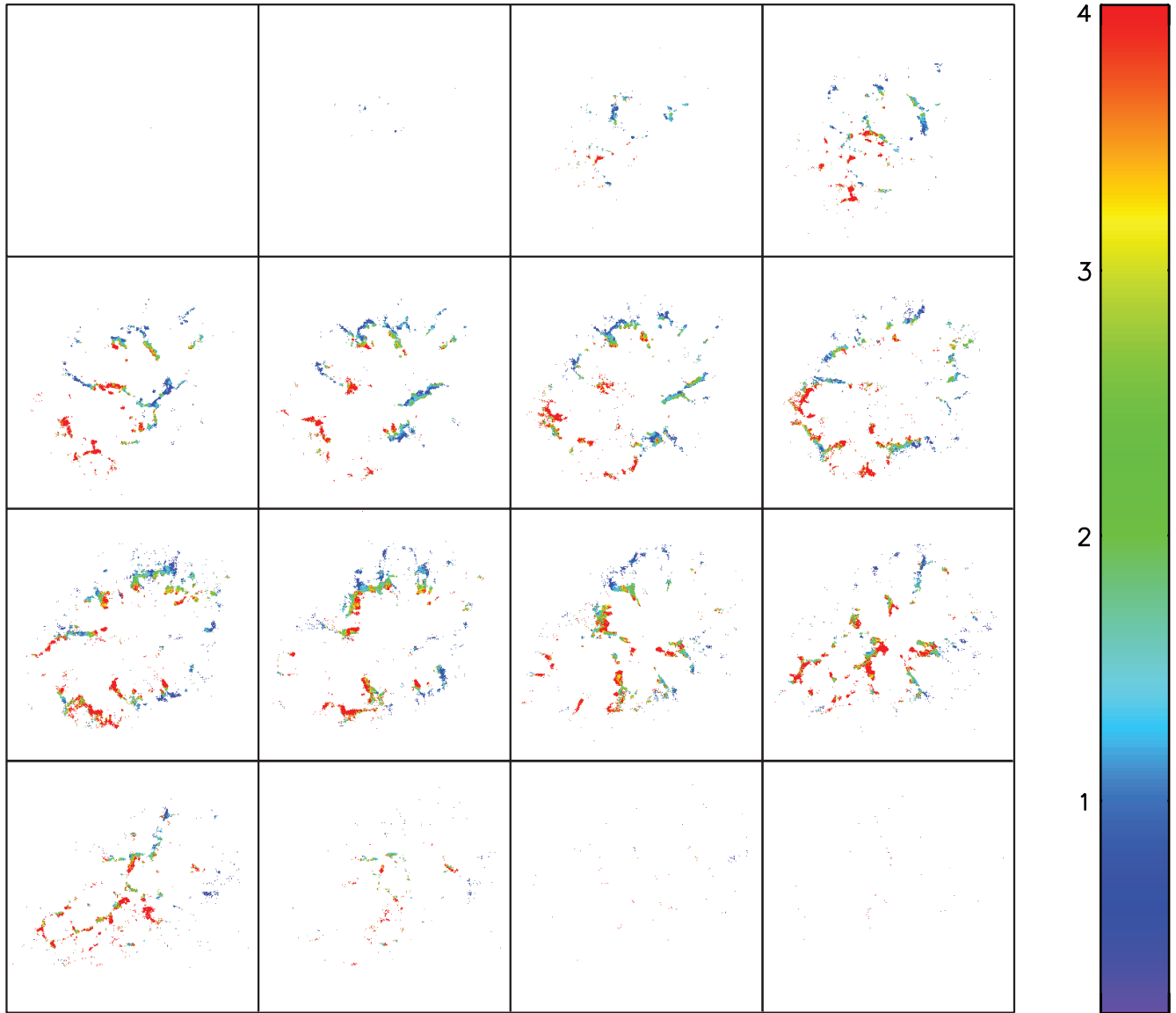


Figure 11. Same as for Figure 10, for the $[\text{S II}]/\text{H}\alpha$ line ratio.
(A full resolution version of this figure is available in the online journal.)

4. ANALYSIS

4.1. Electron Density

Although the electron density of the Crab filaments is a fundamental ingredient in the modeling of this object, systematic determinations of this parameter across the entire nebula have been lacking so far, essentially because of the difficult task of covering the entire nebula with classical spectrographs, but also because of the confusion caused by the overlapping Doppler-shifted filaments. Fesen & Kirshner (1982) have measured electron densities from the ratio of the sulfur lines at ten positions (using short slits), mostly in the outer regions; these vary between 550 cm^{-3} and 1700 cm^{-3} . MacAlpine et al. (1996) measure electron densities that vary between 400 cm^{-3} and 2000 cm^{-3} , without any correlation with the strength of the $[\text{N II}]$ lines. Although Čadež et al. (2004) have obtained a series of long-slit spectra of the Crab and performed spectral deconvolution,

they have not attempted to measure the electron density in the filaments.

Our data cube and deconvolution technique allow us to measure electron densities across the nebula, at least in regions where the signal is sufficient. For a given temperature, the $[\text{S II}] \lambda 6717 / [\text{S II}] \lambda 6731$ line ratio is inversely proportional to the electron density (Osterbrock 1989). Figure 12 shows that the electronic density is relatively constant within a given filament, but varies quite dramatically from one region to another: assuming an electronic temperature of 15,000 K (bounded between 11,000 K and 18,000 K as stated by Henry & MacAlpine 1982) and using the simple FIVEL emission line diagnostic program (De Robertis et al. 1987) we deduce electronic densities varying between $\sim 50 \pm 10 \text{ cm}^{-3}$ and $2500 \pm 200 \text{ cm}^{-3}$. The uncertainties quoted here only reflect the temperature range cited above, and one should remember that the real uncertainties are much higher in the low density regime, where the slope of the line ratio versus electron density curve is very small (Osterbrock 1989).

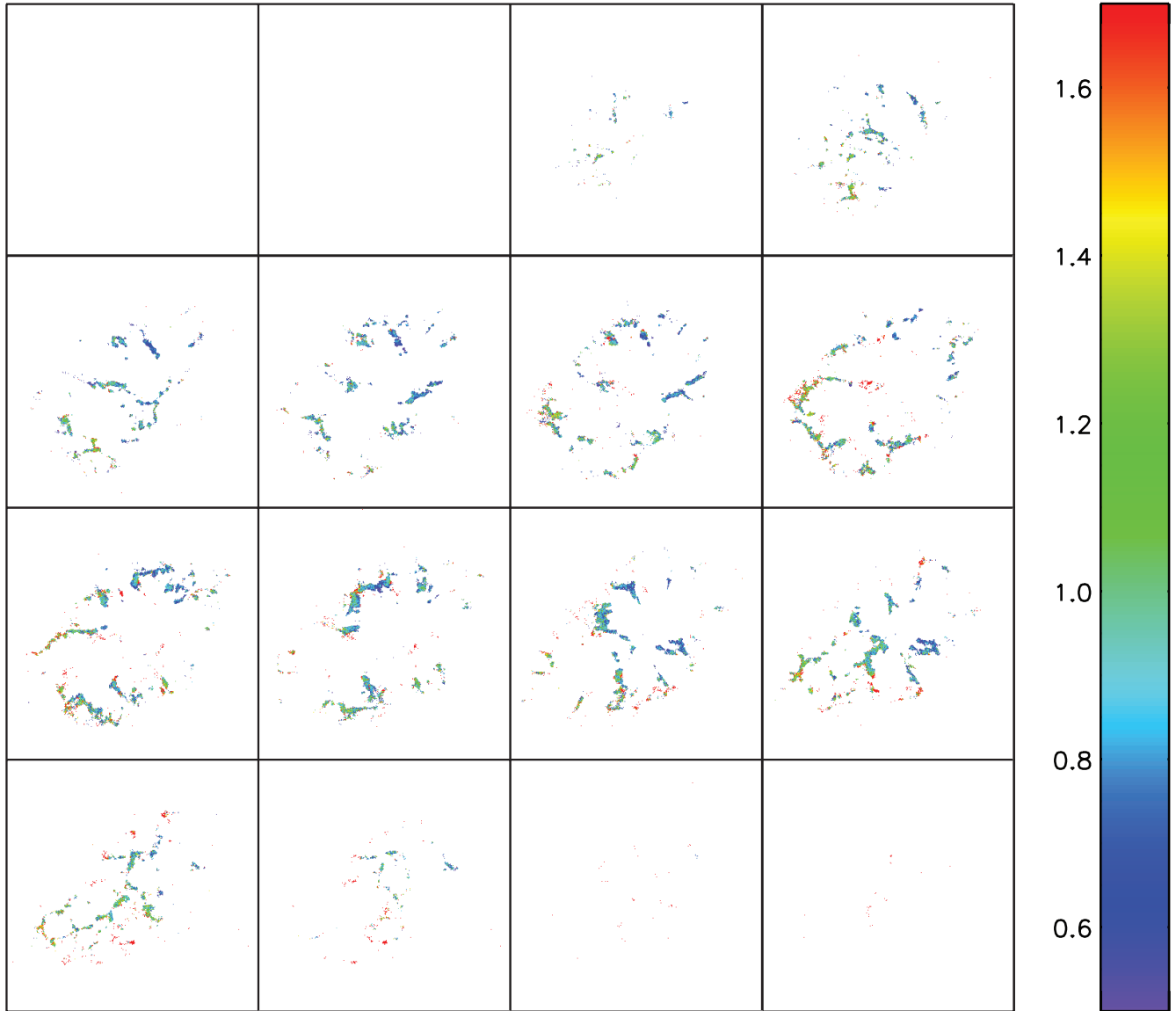


Figure 12. Same as for Figure 10, for the [S II] $\lambda 6716$ /[S II] $\lambda 6731$ line ratio.

(A full resolution version of this figure is available in the online journal.)

We also note that most of the bright, thick, and long structures are relatively dense (bluest areas), while the regions of lower electron density (green, yellow, and red) tend to be thinner. More globally, we observe a definite trend, in the sense that the NW part of the nebula tends to show higher densities than the SE part. Figure 13 quantifies this trend: the average line ratio 2' SE of the pulsar ([S II] 6717/[S II] 6731 ~ 1.1) corresponds to $n_e \sim 600 \text{ cm}^{-3}$, while this ratio goes down to 0.8 1' to the NW, corresponding to $n_e \sim 1400 \text{ cm}^{-3}$. A NW–SE asymmetry has already been noted and discussed by some authors (see Hester 2008) but never has it been systematically established for the electronic density.

4.2. Interpretation of the Density Structure

We now attempt to relate our observation to previous discussions on the NW–SE asymmetry. The filamentary cage-like structure of the Crab is subject to an acceleration (Trimble 1968) due to the pressure exerted of the synchrotron nebula radiating

from the Crab pulsar. Clark et al. (1983) argued that this synchrotron nebula, which is only visible inside the filamentary cage-like structure, must be contained by some mechanism. They proposed to associate it with a skin-like structure surrounding all the bright filaments which would act like a net that prevents the synchrotron nebula from escaping, except in the NW part of the nebula (Velusamy 1984), which seems to be skinless due to leakage of the synchrotron nebula toward that direction.

The structure of the filamentary cage has been the subject of multiple simulations. It is now acknowledged that the light synchrotron plasma, which is pushed into a denser thermal ejecta, is subject to Rayleigh–Taylor (R–T) instabilities (Davidson & Fesen 1985). High spatial resolution *HST* observations revealed a detailed inward finger protrusion structure (Sankrit et al. 1998). Hester et al. (1996) pushed the model a step further by introducing magnetic forces in their R–T protrusion simulations, which are based on the Jun et al. (1995) magnetohydrodynamic calcu-

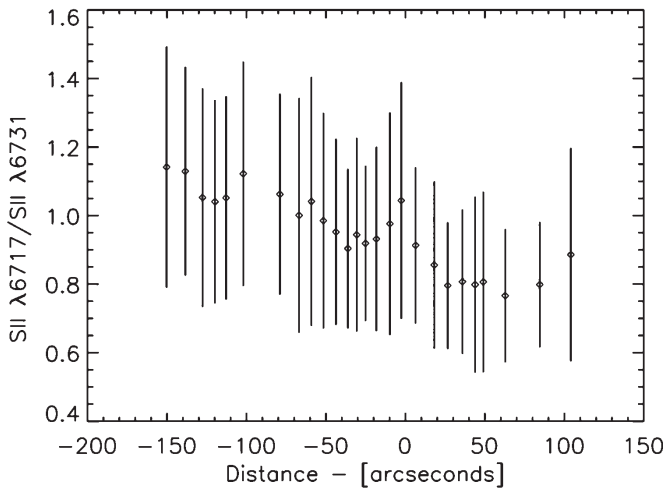


Figure 13. $[S II] \lambda 6717/[S II] \lambda 6731$ ratio as a function of the distance from the pulsar. This plot is obtained by calculations performed on the cube used to generate the map shown in Figure 12. Every voxel that respects the S/N criterion specified earlier is considered. For each voxel, the projected distance on the pulsar axis ($126^{\circ}.31$ east from north; see Ng & Romani 2004) from the pulsar is calculated and the ratio is kept in memory. Every useful voxel is then ordered by its respective distance. Finally, the data are grouped in bundles of 3000 points in ascending distance order. The mean and standard deviation of these bundles are presented above. The standard deviation should be looked as an indicator of the dispersion of the data points, not as an error.

lations. This model explains the formation of the protrusions as leakage of the skin ejecta into the denser and colder protrusions that siphons the material from outside to inside.

Also, as discussed by Loll et al. (2007), the R–T protrusions have a different morphology in the NW region of the nebula. They appear to have spatial wavelengths in the NW part. Since the most probable spatial wavelength of a magnetic R–T protrusion formation is inversely proportional to the density difference between the hot filamentary gas and the synchrotron nebula (see Jun et al. 1995 for some details), it has been suggested that the density in the NW lobe should be lower than the density in the SE part.

However, our direct measurements of the $[S II] \lambda 6717/[S II] \lambda 6731$ ratio indicate the exact opposite, implying that there is another cause to the spatial wavelength difference between the NW and SE lobes. Jun (1998) demonstrated that time is

also a determining parameter of the size of the protrusions. The interpretation we favor is that the NW–SE asymmetry represents a difference in evolutionary stage. The larger filaments in the NW seem to have started to evolve faster than those in the SE part. This interpretation is furthermore consistent with the fact that there is no observable skin within the NW lobe. Since the cold tips of the protrusions drain out the material from the skin (Hester et al. 1996), a more advanced evolutionary stage of the NW lobe could explain why the skin appears worn out in this region.

4.3. $[N II]$ and $[S II]$ Variations

Systematic long-slit spectroscopy by MacAlpine et al. (1996) revealed a significant asymmetry in the $[N II]/H\alpha$ versus $[S II]/H\alpha$ spatial distribution across the Crab. The gas with the strongest $[N II]$ is mostly situated in the NW region while the gas with strongest $[S II]$ is mostly located in the SE region. In their later analysis, MacAlpine et al. (2007) and MacAlpine & Satterfield (2008) revised these data in order to seek possible correlations and argued in favor of variations in abundance distribution across the Crab. They proposed that filaments containing more sulfur would be nitrogen-poor, while filaments containing more nitrogen would be sulfur-poor. The sulfur-rich gas would correspond to more advanced nucleosynthesized matter, but the nitrogen-rich gas was proposed to originate from material that has evolved not much beyond the CNO cycle. Such nitrogen-rich gas would then be strongly associated with the helium mantle, which may have been ejected during successive flashes prior to the core collapse, as suggested by Woosley & Weaver (1986).

Our observations allow us to measure the tridimensional $[N II]$ and $[S II]$ emission distribution where the signal is sufficient. Let us study the $[N II]/H\alpha$ and $[S II]/H\alpha$ ratios maps shown in Figures 10 and 11. It is apparent that their distributions are not the same, as was noted in the literature. In fact, most filaments showing a high $[S II]/H\alpha$ ratio have a low $[N II]/H\alpha$ ratio and vice versa. Figure 14 shows the average ratio of these two elements as a function of the distance along the pulsar axis. The $[N II]/H\alpha$ ratio is clearly higher in the NW part than the $[S II]/H\alpha$ ratio. The exact opposite is observed for the SE lobe. Most of the high $[N II]/H\alpha$ ratio filaments are far from the pulsar, confirming that they have been ejected at higher velocities (MacAlpine et al. 1996) as seen in Figures 10 and 14.

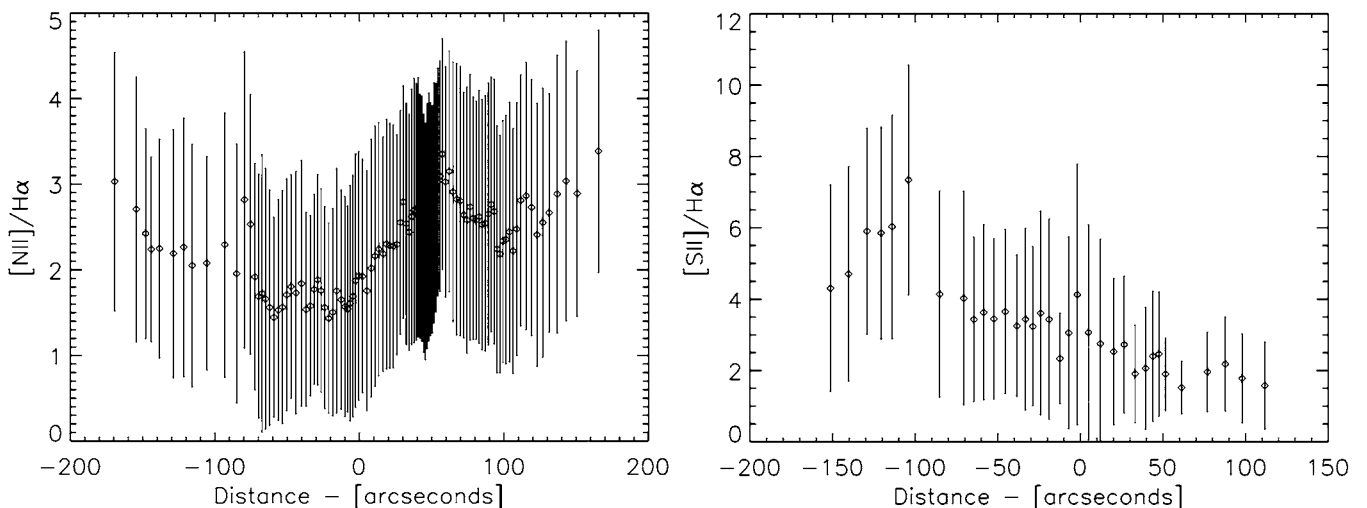


Figure 14. Same as Figure 13, for the $[N II]/H\alpha$ map (left) and the $[S II]/H\alpha$ map (right).

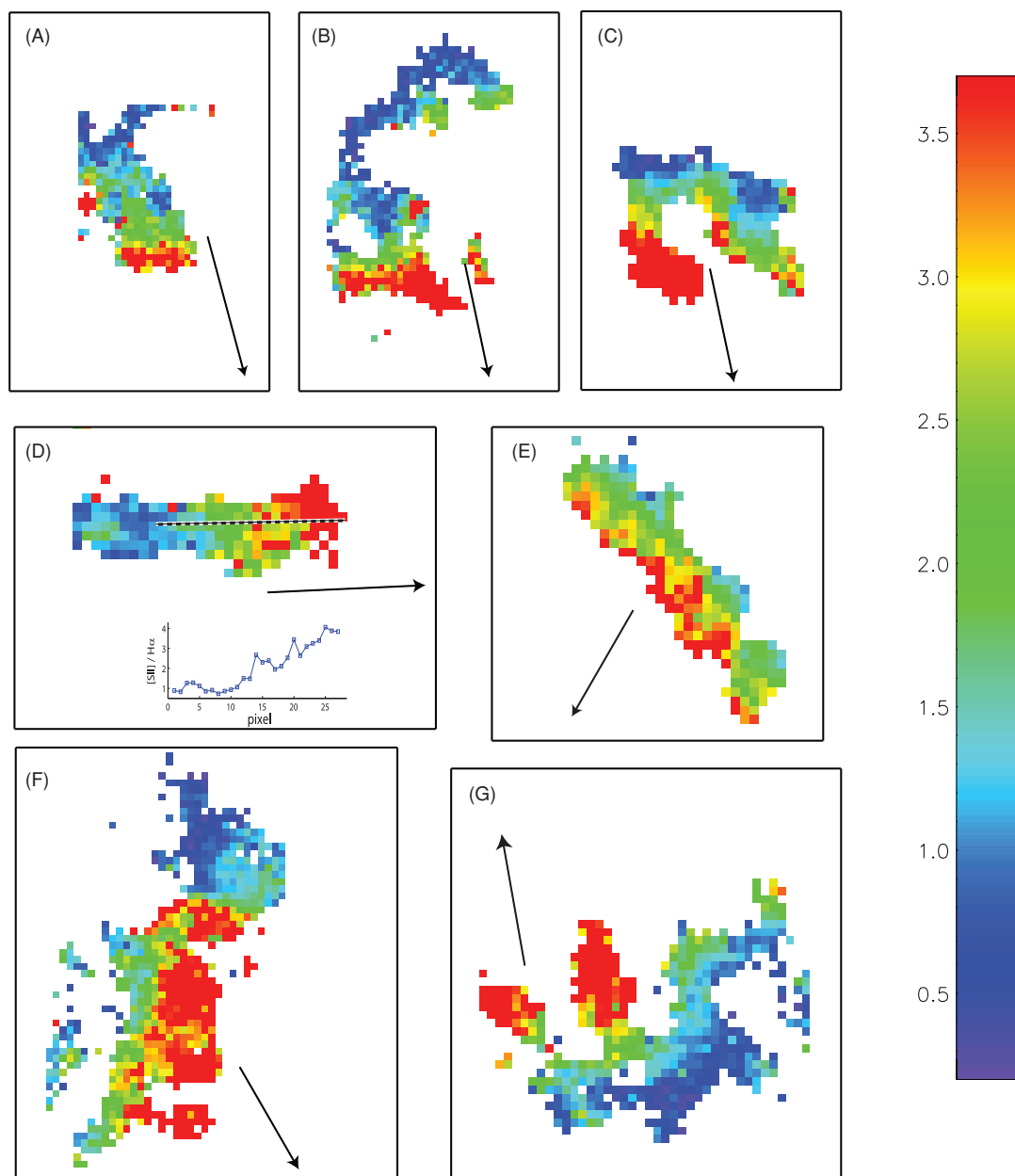


Figure 15. $[S\ II]/H\alpha$ maps for selected filaments identified in Figure 8. In each case, the arrow points towards the pulsar. As it can clearly be seen, there is a strong gradient of the $[S\ II]/H\alpha$ ratio aligned with the pulsar direction revealing that the inner part of a filament is much more shock excited than the outer part. The inset for filament D quantifies this gradient over the filament's length.

If we adopt the suggestion of MacAlpine et al. (1996) that the nitrogen abundance is highly inhomogeneous while assuming that sulfur is more evenly distributed, we may consider that the $[S\ II]/H\alpha$ line ratio is a more reliable shock/photoionization indicator. The higher this ratio is, the more shock-dominated is the emission plasma. The NW–SE asymmetry is clearly apparent in Figures 11 and 14. This asymmetry seems furthermore well correlated with the presence of the skin (Sankrit & Hester 1997), which would act like a net on the synchrotron nebula (except in the NW region). The action of this net would be to restrain the synchrotron nebula and to favor the accumulation of matter, which would flow down into the cooling R–T protrusions. This mechanism, presented in detail by Hester et al. (1996), would generate shocks and thereby favor collisional ionization. Indeed, the skin pouring into the cooler and denser protrusions is expected to generate radiative shocks. Because the NW lobe

is characterized by the absence of any skin, the emission line gas would not be subject to as much collisional ionization.

Some specific filaments have been selected from Figure 11, which reveal interesting trends. These are identified in Figure 8 and are zoomed and presented in Figure 15. As we can furthermore see, there is a strong $[S\ II]/H\alpha$ gradient pointing directly toward the pulsar direction. This means that the interior parts of these filaments are better accounted for by radiative shocks than the outer parts. The interface between the synchrotron nebula and ejecta appears more likely to be collisionally ionized due to the pressure of both the synchrotron nebula and the material being drained into the tips of the inward protrusion. These specific filaments seem to confirm the $[S\ II]/H\alpha$ ratio as a reliable choice shock/photoionization indicator.

We indicated in Section 4.2 that we favor a scenario in which the observed density asymmetry reported in Section 4.1

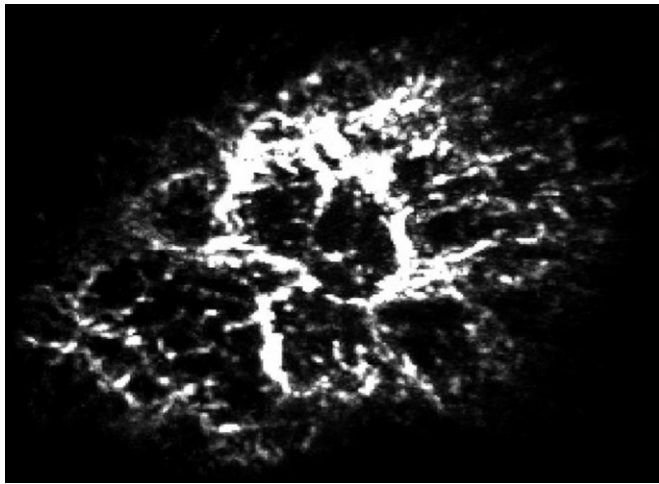


Figure 16. Three-dimensional movie of the Crab nebula, obtained from the $\Omega(v)$ data cube.

(An animation of this figure is available in the online journal.)

is probably the driver of what we perceive as an accelerated evolution of the NW lobe. For instance, a higher density by a factor of ~ 2.3 in the NW must result in a cooling rate ~ 5 times faster in the wake of shock waves, hence, the internal energy injected by the pulsar is exhausted more rapidly (by a factor of ~ 2.3). Furthermore, a higher density can also be expected to accelerate the evolution of the morphological nebular structures, since Jun (1998) demonstrated that time is a determining parameter of the size of the protrusions. If we consider the density as a primordial indicator of the rate at which evolution proceeds, then the NW lobe can be regarded as an “older” region, in which the process of skin plasma flowing into the protrusion is nearly completed, while the SE lobe, which is characterized by a lower density, would hence be “younger” and less evolved, with matter still flowing down into the protrusions, which results in more internal shocks.

It is important to emphasize that the proposed interpretation is foremost a coherent hypothesis of plausible mechanisms responsible in our view for the $[\text{S II}]/\text{H}\alpha$ distribution. An alternative explanation of Figure 15 could be that heavier elements like sulfur were pushed outward into the filaments by a relativistic wind (MacAlpine et al. 2007). Tridimensional temperature measurements of the individual filaments (from the $[\text{O III}]\lambda 4363/[\text{O III}]\lambda 5007$ line ratio, for instance) would be needed to confirm the shock/photoionization interpretation.

5. A THREE-DIMENSIONAL MODEL OF THE CRAB

A last important feature that can be extracted from these observations is a tridimensional structure of the Crab nebula. Despite the fact that only two dimensions of the cube are spatial while the third is kinematical, it has nevertheless been possible to construct a three-dimensional structure movie of the Crab using the XRAY package, from the Karma visualization tool (Gooch 1996). In the electronic version of this paper (Figure 16), we present a movie of the $\Omega(v)$ cube. In addition to be a by-product of our data analysis, this cube presents a good visualization of the most probable radial velocity of the bright emission ejecta filaments in the light of the $\text{H}\alpha$, $[\text{N II}]$, and $[\text{S II}]$ lines. The right-hand panel of Figure 7 represents a slice through the $\Omega(v)$ cube, where the three-dimensional structure is more explicitly revealed. It provides an intuitively easy-to-interpret movie since

it reveals a more precise view of the filaments widely spread in velocity than our line-fitting technique result. By assuming a constant expansion velocity over time since the moment of the Crab supernova explosion, the resulting velocity cube can be regarded as a reliable tracer of three-dimensional physically connected structures.

6. CONCLUSIONS

We have presented the first scientific data obtained with the imaging FTS SpIOMM. We first demonstrate the reliability of SpIOMM by comparing various data with previously published observations obtained with traditional spectrometers and imagers. The unique wide-field hyperspectral potential of SpIOMM is particularly well suited to study the complexity of the kinematical structures in the Crab nebula.

The red data cube was analyzed using a deconvolution technique in order to calculate the tridimensional map of $[\text{N II}]/\text{H}\alpha$, $[\text{S II}]/\text{H}\alpha$, and $[\text{S II}]\lambda 6717/[\text{S II}]\lambda 6731$ ratios. The truly new aspect of these new data is that they allow us to derive a reliable tridimensional photoionization and electronic density maps of this supernova remnant which imply strong constraints for any model that aims at deeper understanding of the emission processes at play in the Crab. In particular, the ionization process and the density structure distribution have been deduced and both show a clear strong NW–SE asymmetry, and reveal that the skin-less NW lobe appears to have evolved faster than the SE part. These characteristics are possibly related to a fundamental asymmetry in the explosion mechanism itself (Burrows et al. 2007).

L.D. is grateful to the Canada Research Chair program, the Natural Sciences and Engineering Research Council of Canada (NSERC), the Canadian Foundation for Innovation (CFI) and the Fonds Québécois de la Recherche sur la Nature et les Technologies (FQRNT) for financial support. M.C. and A.P.B. also thank NSERC and FQRNT for financial support. L.B. acknowledges financial support from CONACyT grant J-50296. SpIOMM is the result of a collaboration between Université Laval and ABB Bomem Inc., and has been funded by NSERC, CFI, FQRNT, and the Canadian Space Agency. Comments from an anonymous referee were very helpful to improve the quality of the paper.

REFERENCES

- Bernier, A.-P., et al. 2008, *Proc. SPIE*, **7014**, 70147J
- Burrows, A., Dessart, L., Ott, C. D., Livne, E., & Murphy, J. 2007, in IAU Symp. 250, *Massive Stars as Cosmic Engines*, ed. F. Bresolin, P. A. Crowther, & J. Puls (Cambridge: Cambridge Univ. Press), 185
- Čadež, A., Carramiñana, A., & Vidrih, S. 2004, *ApJ*, **609**, 797
- Clark, D. H., Murdin, P., Wood, R., Gilmozzi, R., Danziger, J., & Furr, A. W. 1983, *MNRAS*, **204**, 415
- Davidson, K., & Fesen, R. A. 1985, *ARA&A*, **23**, 119
- De Robertis, M. M., Dufour, R. J., & Hunt, R. W. 1987, *J. R. Astron. Soc. Canada*, **81**, 195
- Drissen, L., et al. 2008, *Proc. SPIE*, **7014**, 70147K
- Fesen, R. A., & Kirshner, R. P. 1982, *ApJ*, **258**, 1
- Grandmont, F., Drissen, L., & Joncas, G. 2003, *Proc. SPIE*, **4842**, 392
- Gooch, R. 1996, in ASP Conf. Ser. 101, *Astronomical Data Analysis Software and Systems V* (San Francisco, CA: ASP), 80
- Henry, R. B. C., & MacAlpine, G. M. 1982, *ApJ*, **258**, 11
- Hester, J. J. 2008, *ARA&A*, **46**, 127
- Hester, J. J., et al. 1996, *ApJ*, **456**, 225
- Jun, B.-I. 1998, *ApJ*, **499**, 282
- Jun, B.-I., Norman, M. L., & Stone, J. M. 1995, *ApJ*, **453**, 332

- Kastra, J. S., de Vries, C. P., Costantini, E., & den Herder, J. W. A. 2009, [A&A](#), **497**, 291
- Lawrence, S. S., et al. 1995, [AJ](#), **109**, 2635
- Loll, A. M., et al. 2007, AAS Meeting, **211**, 100.25
- MacAlpine, G. M., Ecklund, T. C., Lester, W. R., & Vanderveer, S. J. 2007, [AJ](#), **133**, 81
- MacAlpine, G. M., Lawrence, S. S., Sears, R. L., Sosin, M. S., & Henry, R. B. C. 1996, [ApJ](#), **463**, 650
- MacAlpine, G. M., & Satterfield, T. J. 2008, [AJ](#), **136**, 2152
- Ng, C.-Y., & Romani, R. W. 2004, [ApJ](#), **601**, 479
- Noel, B., Joblin, C., Maillard, J. P., & Paumard, T. 2005, [A&A](#), **436**, 569
- Osterbrock, D. E. 1989, *Astrophysics of Gaseous Nebulae and Active Galactic Nuclei* (Mill Valley, CA: Univ. Science Books), 439
- Paumard, T., Maillard, J.-P., & Morris, M. 2004, [A&A](#), **426**, 81
- Rola, C., & Pelat, D. 1994, [A&A](#), **287**, 676
- Sankrit, R., & Hester, J. J. 1997, [ApJ](#), **491**, 796
- Sankrit, R., et al. 1998, [ApJ](#), **504**, 344
- Storey, P. J., & Zeppen, C. J. 2000, [MNRAS](#), **312**, 813
- Temim, T., et al. 2006, [AJ](#), **132**, 1610
- Trimble, V. 1968, [ApJ](#), **73**, 535
- Velusamy, T. 1984, [Nature](#), **308**, 251
- Woosley, S. E., & Weaver, T. A. 1986, [ARA&A](#), **24**, 205